ADM-Aeolus retrieval algorithms for aerosol and cloud products

P.-H. Flamant, J. Cuesta, Marie-Laure Denneulin, Alain Dabas, Dorit Huber

Tellus (2008), 60A, 273–286
Printed in Singapore. All rights reserved

TELLUS

ADM-Aeolus retrieval algorithms for aerosol and cloud products

By PIERRE FLAMANT[1]*, JUAN CUESTA[1], MARIE-LAURE DENNEULIN[2], ALAIN DABAS[2] and DORIT HUBER[3], [1]*Laboratoire de Météorologie Dynamique/Institut Pierre Simon Laplace, École Polytechnique, 91128 Palaiseau, France;* [2]*Météo-France, Toulouse, France;* [3]*Deutsches Zentrum für Luft- und Raumfahrt, Oberpfaffenhofen, Germany*

(Manuscript received 15 January 2007; in final form 4 September 2007)

ABSTRACT

ADM-Aeolus, the wind Lidar under development at ESA, is a High Spectral Resolution Lidar that additionally provides separated information on particles (Mie channel) and molecules (Rayleigh channel). Lidar signals will be accumulated in vertical range bins in order to reach sufficient signal-to-noise ratio for reliable wind estimates. The vertical range bin integration may vary from 250 m near the surface up to 2 km in the upper troposphere and lower stratosphere. Significant attenuation in a range bin changes the nature of the retrieval problem. The commonly used Lidar inversion techniques appear to be inadequate to process bin-accumulated signals. This paper presents the 'L2A processor', conceived to use ADM-Aeolus signals to provide information on aerosol and cloud layers optical properties. The altitude, geometrical depth, optical depth, backscatter-to-extinction ratio and scattering ratio are to be retrieved. The L2A processor algorithms provide a new formulation to the inverse problem for various filling cases of a range bin and it includes a credibility criterion (CC) in order to select the best filling approximation. The effective vertical resolution can be two to four times better than the ADM-Aeolus range bins. The basic concept, the processing algorithms, numerical examples and sensitivity tests are here presented.

1. Introduction

The Atmospheric Dynamics Mission ADM-Aeolus is the fourth of ESA's Earth Explorer Missions[1] (ESA, 1999; Stoffelen et al., 2005). ADM-Aeolus is scheduled for launch in mid 2009 and has a projected lifetime of 3 yr. ADM-Aeolus is a pulsed Lidar operating in the UV range at 355 nm. It has the capability to profile the dynamical, structural and optical properties in the lower atmosphere. Its primary objective is to demonstrate the capability to measure wind profiles from space using ALADIN, a Doppler Wind Lidar (DWL). According to the basic instrumental design, ALADIN on ADM-Aeolus is a High Spectral Resolution Lidar (HSRL) that implements two separate channels for the detection of the laser light scattered by molecules and particles (Shipley et al., 1983; Imaki et al., 2005). The two channels enable the retrievals of wind from particle free atmosphere (air molecules mostly) and cloud/aerosol layers, respectively. For a HSRL configuration provides with two independent Lidar signals from (i) molecules and (ii) particles, it enables also to retrieve unambiguously the optical properties of clouds and aerosols, contrary to standard elastic backscatter Lidar (SEBL). This capability to perform monitoring of cloud/aerosol layer optical properties is essential in the framework of the present paper in the continuation of the CALIPSO joint NASA/CNES mission launched in April 2006 (Winker et al., 2003). However, vertical resolution of ADM-Aeolus signals is coarse (from 500 to 2000 m). This limitation implies the development of a new inversion technique, the so-called L2A processor, which is the main issue addressed in this paper.

As an introduction to the present paper, the difference between HSRL and SEBL is outlined below. A SEBL collects and detects together the laser light scattered by molecules and particles. The SEBL signal strength $s(R)$ as a function of range R is

$$s(R) = K\ R^{-2}[\beta_m(R) + \beta_p(R)] \times \exp\left\{-2\int_0^R \left[\alpha_m(y) + \alpha_p(y)\right] \mathrm{d}y\right\}. \quad (1)$$

The instrument constant K is function of the transmitted laser energy, receiver telescope diameter, overall optical efficiency and photo detector efficiency. The backscatter coefficient β (in $\mathrm{m}^{-1}\ \mathrm{sr}^{-1}$) and the extinction coefficient α (in m^{-1}) stand for air molecules and particles with subscripts m and p, respectively. The instrumental parameters and units are listed

*Corresponding author.
e-mail: flamant@lmd.polytechnique.fr
DOI: 10.1111/j.1600-0870.2007.00287.x
[1]ESA Earth Explorers web site: www.esa.int/esaLP/LPearthexp.html.

Table 1. Comparison of the main characteristics of the space borne Lidar ALADIN and CALIOP onboard ADM-Aeolus and CALIPSO platforms, respectively

Mission	ADM-Aeolus	CALIPSO
Lidar	ALADIN HSRL	CALIOP SEBL
Nd-YAG laser operating wavelength(s)	355 nm	532–1064 nm
Transmitted energy per pulse	150 mJ	110 mJ (at both wavelengths)
Laser polarization	Linear	Linear
Pulse duration	30 ns	20 ns
Pulse repetition frequency	100 Hz	20 Hz
Receiver telescope diameter	1.5 m	1 m
Receiver field-of-view (full angle)	18 μrad $\times$ 30 the diffraction limit	130 μrad $\times$ 200 the diffraction limit
Multiple channel receiver	(a) Rayleigh: Dual Fabry–Perot interferometer for light scattered by air molecules	(a) 532 nm // polarized
	(b) Mie: Fizeau interferometer for light scattered by particles	(b) 532 nm $\perp$ polarized
		(c) 1064 nm
Receiver spectral bandwidth	(a) 0.7 pm for Rayleigh channel	(a) and (b) 35 pm (at 532 nm)
	(b) 0.06 pm for Mie channel	(c) Standard interference filter (at 1064 nm)
Vertical resolution (range bin)	500, 1000, 2000 m	30 m
Horizontal resolution (on satellite track)	3.8 km (measurement) 50 km[b] (observation) void of 150 km every 200 km	330 m (measurement) 26.4 km[b] (observation) continuous sampling
Pointing of line-of-sight	35° off-nadir	From 0 to 3° tilt off nadir (to cancel spurious reflections)
Orbit height	400 km (496 km range)	705 km
Lidar footprint at surface	9 m	92 m

[a]Horizontal resolution may be better depending on actual SNR.

[b]Estimation using actual CALIPSO 532 nm // level 1 signals to keep daytime SNR>3 and nighttime SNR>6.

in Table 1. Equation (1) is derived assuming single scattering approximations (SSA). In presence of so-called multiple scattering effects (MSE) in dense particle layers or due to strong forward scattering by large particles, a MSE correcting factor $0 \leq \eta \leq 1$ is used and the exponential term writes $\eta \int_0^R \alpha_p(y)\,\mathrm{d}y$ for particles. However, even such a simple approximation for MSE is a source of ambiguity in the retrieval of particle optical properties. A large number of studies have been devoted to estimate the importance of MSE on Lidar retrievals with respect to SSA, as a function of the receiver telescope field-of-view (FOV), extinction coefficient and range to the scattering layer (Nicolas et al., 1997; Mitrescu, 2005).

A discussion in depth of MSE on Lidar retrievals is beyond the scope of the present paper. However, one can say that in many situations relevant to Earth radiation budget issues the SSA applies on ADM-Aeolus retrievals. Among others, one issue addresses the importance of thin cirrus clouds for they can result in a cooling or warming effect depending on their optical and microphysical properties and altitude (i.e. temperature). In order to address the importance of MSE and the relevance of SSA, we consider the following parameters for ADM-Aeolus: emission wavelength $\lambda \cong 355$ nm, range to the surface $R \cong 500$ km, receiver full FOV $\cong 18$ μrad (see Section 2), and $\alpha_p \cong 0.5$–2 km^{-1}. First, based on the theory presented in Nicolas et al. (1997), our numerical applications show that the SSA is valid ($\eta \cong 1$) for aerosols and clouds with particle diameters $d_p \leq 10$ μm. For larger particles (e.g. cirrus clouds), it applies for $d_p \cong 35$ μm and moderate extinction coefficient (<1 km^{-1}). For $d_p \cong 100$ or 350 μm, the SSA applies only for small optical depth OD ≤ 0.3 (e.g. thin cirrus clouds) that result in independent forward scattering (i.e. only a small fraction of the forward diffraction peak is contained in the receiver FOV).

It remains that for large particles and large OD the MSE are significant and they need to be taken into account through η in eq. (1). Because the particle size is not known a priori the retrieval problem is complex for large particles associated to large OD. The issue will be addressed in a future study using Monte Carlo simulations. Additionally, no error propagation effects associated to MSE has been verified that result of the newly proposed retrieval algorithm (see Section 5).

One single eq. (1) involves the two unknowns of interest $\beta_p(R)$ and $\alpha_p(R)$. β_m and α_m can be computed from meteorological information, that is, pressure $p(z)$ and temperature $T(z)$, as a function of altitude z as follows

$$\beta_m(z) = 1.38 \times 10^{-6} \left(\frac{550}{\lambda}\right)^{4.09} \left[\frac{p(z)}{1013}\,\frac{288}{T(z)}\right] \mathrm{m}^{-1}\ \mathrm{sr}^{-1}, \tag{2}$$

where λ in nm is the probing laser wavelength (355 nm for ADM-Aeolus). The molecular extinction coefficient is computed according to $\beta_m(z) = k_m \alpha_m(z)$, where $k_m = 3/8\ \pi \cong 0.118$ (in sr^{-1}) is constant from the surface up to an altitude of 80 km. The relative errors on molecular coefficients scale with uncertainties on temperature (1 K $\Rightarrow$ 0.3%) and pressure (1 hPa $\Rightarrow$ 0.1%). The coefficient α_p (or β_p) can be retrieved from eq. (1) and $s(R)$ as long as α_p and β_p may be connected together, in order to deal with one single unknown. A linear relationship $\beta_p(z) = k_p \alpha_p(z)$ based on scattering theory is usually used (Fernald et al., 1972; Fernald, 1984). Even so, k_p is an issue because it depends on many parameters such as the composition of particle mixture, particle size, shape, orientation and refractive index (Carier et al., 1967; Evans, 1988; Ackerman, 1997; Noel et al., 2001). In practice, k_p values may span by one order of magnitude ($k_p < k_m$). It may vary as a function of range, but in practice a mean value is used (Fernald et al., 1972; Fernald, 1984). For an SEBL like CALIPSO, k_p must be known a priori before signal processing. It is provided as an auxiliary data set. On the contrary, ADM-Aeolus can provide with unambiguous solutions (see Section 7).

The two basic HSRL equations for laser light scattered by molecules and particles as a function of range are, respectively,

$$s_m(R) = K_m\ R^{-2} \beta_m(R)\ \exp\left\{-2 \int_0^R [\alpha_m(y) + \alpha_p(y)]\ \mathrm{d}y\right\} \tag{3a}$$

$$s_p(R) = K_p\ R^{-2}\ \beta_p(R)\ \exp\left\{-2 \int_0^R [\alpha_m(y) + \alpha_p(y)]\ \mathrm{d}y\right\}. \tag{3b}$$

Note molecules and particles attenuate the collected light in the two channels, whereas scattering is due to either molecules or particles. The variables in eqs. (3a) and (3b) have the same meaning as in eq. (1). Equations (3a) and (3b) could involve a MSE correcting factor for large particles with large OD as discussed previously. Equations (1), (3a) and (3b) stand for Lidars operating from the ground, aircraft and space platforms.

ADM-Aeolus will provide with bin-accumulated Lidar measurements in 25 range bins. It is worth to notice that a significant attenuation within a range bin changes the nature of the HSRL equations and the solution. It calls for a new processing algorithm. In this paper, we describe the ADM-Aeolus Level-2A (L2A) spin-off products retrieval algorithms for cloud and aerosol optical properties i.e. optical depth, k_p and scattering ratio (the ratio between the total backscatter by particles and molecules and the molecular backscatter). The L2A algorithms take into account the technical constraints with respect to vertical and horizontal sampling (see Table 1). Product confidence indicators are important items that will be provided with the retrievals. The ADM-Aeolus mission is presented in Section 2. The scope and purpose of the L2A processor are presented in Section 3. Bin-accumulated HSRL signals are discussed in Section 4. The L2A processing algorithm for the Rayleigh channel is provided in Section 5. Examples illustrating the performance of the proposed new algorithm are provided in Section 6. The L2A processing algorithm for the Mie channel and synergism between the Mie and Rayleigh channels are provided in Section 7.

2. ADM-Aeolus mission

ADM-Aeolus will provide two simultaneous measurements from molecules and particles (see eqs 3a and 3b) with further bin-accumulation at CCD detector level. The current baseline configuration for the 25 range bins will provide 1000 m vertical accumulation through most of the lower atmosphere (from 2 to 16 km), 500 m below 2 km mostly in the atmospheric boundary layer and 2000 m between 16 and 26 km in the stratosphere. The two top range bins (#25 and #24) will be used for instrumental purpose and calibration, respectively. The ADM-Aeolus instrument is viewing from a low-altitude ($\sim$400 km) polar orbit in the direction perpendicular to the satellite track (Fig. 1). The polar orbit facilitates global data coverage, required for numerical weather prediction (NWP) and climate applications. There is only information on the line-of-sight (LOS) at the local elevation angle ($\sim 63^\circ$), which is close to east–west except at high latitudes (for comparison, CALIPSO is looking at nadir or a few degrees off nadir). ADM-Aeolus will typically provide approximately 50-km-average observations[2] in horizontal or at a better horizontal resolution when the signal strength will be sufficient (i.e. signal-to-noise ratio SNR > 10) separated by voids of 150 km data gaps. Such a duty cycle of 25% and resulting sampling in the atmosphere is driven for science to ensure minimal error correlation between consecutive wind observations (Stoffelen et al., 2005) and satellite technical considerations to maximize the information content while conserving the energy consumption of ALADIN. The accuracy on the retrieved ADM-Aeolus aerosol and cloud spin-off products will primarily depend on SNR, which in turn is driven at instrument level by k_m and k_p (eqs. 3a and 3b).

Regarding the aerosol/cloud products to be retrieved by ADM-Aeolus, it is worth to say that even for a limited vertical resolution, but taking advantage of the HSRL capability, the continuity of Lidar measurements from space after CALIPSO is essential. A long term data base on aerosol/cloud products will help to better understand the role of aerosols and clouds on Earth radiative budget and climate change. Table 1 provides information for comparison on the ALADIN and CALIOP Lidars, onboard the ADM-Aeolus and CALIPSO platforms, respectively.

[2]The term 'measurement' is used for instrument data characterized by horizontal scales of between 1 and 10 km, whereas 'observation' is used for aggregated data at horizontal scales of 50 km.

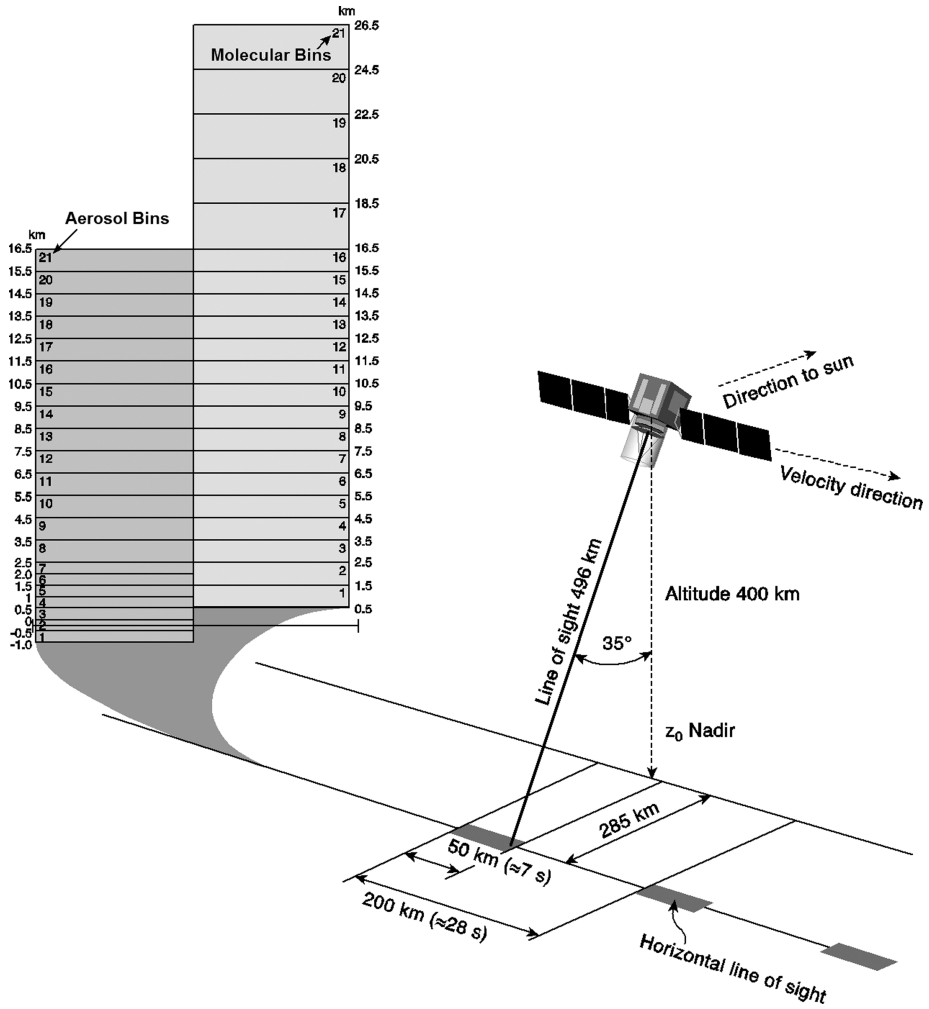

Fig. 1. Line-of-sight viewing geometry and proposed verticals distribution of the range bins for the ADM-Aeolus satellite, showing vertical sampling by the particle (Mie) and molecular (Rayleigh) channels separately (see also Table 1).

The implementation of the ADM-Aeolus receiver is dictated by the scattered light spectrum characteristics (see Fig. 2). It is made of a narrow line associated to particles and a broad nearly Gaussian line shape associated to molecules. The two spectra are centred at the same frequency and the central frequencies sweep together according to the Doppler frequency shift (as a function of radial velocity). In order to split the two contributions into two distinct spectra the ALADIN instrument implements a narrow line shape Mie receiver (a Fizeau interferometer) and a broader line shape Rayleigh receiver [a dual Fabry Perot interferometer (Chanin et al., 1989; Garnier and Chanin, 1992)]. The molecular spectrum bandwidth varies with height in the atmosphere, with temperature mainly and pressure to a lesser degree. In the lower atmosphere a Brillouin doublet occurs on the two sides of the broad Gaussian shape line that results in a Rayleigh–Brillouin line shape (Boley et al., 1972; Tenti et al., 1974; Pan et al., 2004). The impact of Rayleigh–Brillouin spectrum on the optical property retrievals is limited and can be addressed satisfactorily by calibration using a so-called Tenti S6 model (Tenti et al., 1974; Flamant et al., 2005). The Mie receiver does not resolve the scattered spectrum by particles. The Rayleigh receiver is made of two band-pass filters set on both sides of the broad molecular spectrum ('A' and 'B' in Fig. 2). The relevant information is the number of collected photons N_A and N_B in each subchannel. The ratio $[(N_A - N_B)/(N_A + N_B)]$ is a function of the Doppler frequency shift and it enables to derive the radial wind velocity along the LOS. In order to maximize the optical efficiency, the overall receiver design is rather complex based on polarization discrimination effects before detection. The atmospheric signal first enters the Mie receiver and subsequently the Rayleigh receiver. An inherent cross-talk exists between the Mie and Rayleigh channels, for on the one hand the dual Fabry–Perot subchannels A and B may collect a fraction of the spectrum associated to particles (it will depend on signal strength and so on scattering ratio), whereas on the other hand the Fizeau interferometer collect a fraction of the central portion of the molecular

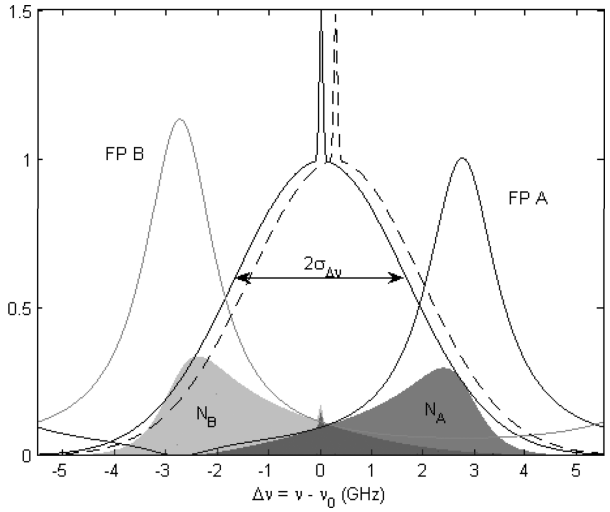

Fig. 2. Scattered spectrum by molecules (broadband) and particles (narrow line) and transfer function of the Dual-Fabry–Perot interferometer (DFPI) implemented in the Rayleigh channel receiver. A typical atmospheric spectrum is displayed by the black solid line. The spectrum is centered about the central frequency of the transmitted laser pulse (here taken as reference '0'). The transmission transfer functions of two sub channels A (right) and B (left) of the DFPI are displayed as deep grey (FP A) and light grey (FP B) solid lines, respectively. They are representative of the nominal design of the Rayleigh channel receiver. The deep grey and light grey shaded areas are proportional to the useful number of photons N_A and N_B before detection. If the spectrum is positively Doppler shifted (see the black dashed line) by 282 MHz associated to a 50 m s^{-1} radial velocity in this example, N_A increases while N_B decreases and $N_A + N_A$ stays nearly constant so the Rayleigh response $R_R = (N_A - N_B)/(N_A + N_B)$ increases.

spectrum that can be regarded as one additional component to solar background light (see Section 4). The cross-talk needs to be taken into account by a proper calibration (see Sections 4 and 6). Moreover, light reflected from the Mie channel's Fizeau interferometer, that may enter the Rayleigh channel, needs to be taken into account.

A narrow FOV for ADM-Aeolus is dictated by the performance of the interferometers. A small FOV results in a footprint of 9 m at surface and a footprint to range ratio of 1.8×10^{-5} compared to 92 m and 13×10^{-5} for CALIPSO. For spaceborne Lidars, the importance of MSE on the retrievals scales with Lidar footprint (the smaller the better). In most cases, the MSE are expected to be limited if not negligible for ADM-Aeolus (except for the case of large particles and high OD; see Section 1). In this respect, ADM-Aeolus has better performance than CALIPSO. A narrow FOV still much larger than the diffraction limit precludes signal fluctuations due to speckle effects.

3. L2A processor

The L2A algorithms are designed to retrieve the cloud and aerosol optical properties at a 3.8-km (one measurement) to 50-km scale (one observation). They are derived primarily to form part of a piece of software that creates the ADM-Aeolus Level-2A (L2A) data products, based on the calibrated measurements (L1B) as inputs. Given the experimental nature of the mission, it has been recognized that data processing needs to have sufficient flexibility to explore the full potential of the mission. The L2A spin-off retrieval algorithms are likely to evolve during the mission. The evolution is expected to be relatively minor, but of course any changes will be thoroughly documented. The L2A software will be freely available for the atmospheric community. As it stands today, the spin-off products do not need to be processed in real time and the issue will not be discussed here, but the software will be designed to be portable.

L1B data are the input to the L2A processor. For one active period of approximately 50 km (Fig. 1), the L1B data set is a matrix of [14 columns (j) $\times$ 24 rows (i)], obtained from on-board analogue accumulation. Each of the $N_{mes} = 14$ columns is an atmospheric profile at the measurement scale, acquired by accumulation of $N_{shots} = 50$ laser returns. The $N_{range} = 24$ rows correspond to the vertical range bins. Given the satellite ground-velocity of $\sim$7.6 km s^{-1} and a pulse repetition frequency (PRF) of 100 Hz, each one of the N_{mes} measurements integrates the atmospheric returns over a horizontal distance of 3.8 km. A 3.8-km scale will give access on atmospheric heterogeneities within one observation to identify those situations that may lead to aberrant measurements or representativity errors in the retrievals (i.e. instabilities in signal calibration, improper averaging of a highly heterogeneous atmosphere, etc.). It could be further averaged up to 50 km depending on signal-to-noise ratio (SNR). One orbit is made of about 200 independent pieces of data.

Figure 3 presents the L2A algorithms. As a first step, a 'Feature Finder' algorithm based on Mie channel information, that is, light scattered by particles (narrow line spectrum), identifies the range bins that contains particles and computes a scattering ratio, using the narrow line component and molecular background after subtraction of the solar background (first guess). This information will be used to make a distinction between (i) clear air and (ii) cloud/aerosol layers. For each range bin i, measurements at a 3.8-km scale will be used to derive the fraction of cloud or aerosol layers (not discriminated at this point) in the 50-km observations. The 'Processing Algorithms' are designed to retrieve for each range bin i the: (i) particle local optical depth $LOD_{p,i}$ or equivalently a 'mean' extinction coefficient for particles $\alpha_{p,i,}$, (ii) backscatter-to-extinction ratio for particles $k_{p,i}$ and (iii) scattering ratio $R_{sca,i}$. The auxiliary data sets on Fig. 3 will be used for signal processing on-ground. The very basic needs, as outlined in Section 1 and further presented in Section 4, are the atmospheric temperature and pressure profiles for processing of the Rayleigh channel signals and k_p^{aux} for processing of the Mie channel signals (in the event the Rayleigh channel is not available). The meteorological variables i.e. pressure, temperature, relative humidity, cloud cover, water/ice content, will be provided by Global Circulation Models (GCM) analysis. A

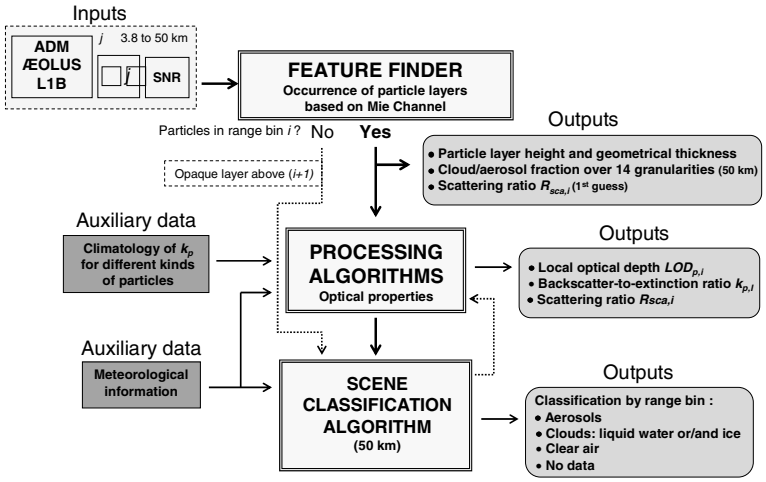

Fig. 3. Basic concept of the L2A algorithm to retrieve aerosol and cloud properties using ADM-Aeolus data, geophysical variables provided by GCM analysis and microphysical properties for particles. A granularity (i, j) is tagged with 2 indices i for vertical (column) and j for horizontal (row), respectively.

Table 2. Comparison of retrieval capabilities by ADM-Aeolus and CALIPSO according to on-board measurements

Mission	Spatial sampling	Particle layer detection (Feature finder)	Optical properties	Scene classification
ADM-Aeolus *HSRL*	Poor in vertical. It may be improved with new L2A algorithm.	Good. Mie channel performs well even at moderate SNR.	Good. It uses full HSRL capability to derive LOD_p and k_p.	Limited. One/two pieces of information provided by Lidar (LOD_p and k_p). No complementary payload instrument.
CALIPSO *SEBL*	Good. Continuous sampling in horizontal and vertical. But it may require averaging in case of low SNR.	Fairly good provided SNR is high enough. Otherwise, it may require averaging.	Fairly good. It includes colour ratio and depolarization ratio. But a priori knowledge of k_p results in ambiguity on LOD_p.	Good. Several pieces of information by Lidar and synergism with on-board IIR and WAC.

HSRL: high spectral resolution Lidar, SEBL: Standard elastic backscatter Lidar, IIR: infrared imager, WAC: wide angle camera.

database for k_p at 355 nm is under progress at ESA, while a database for k_p at 532 nm and 1064 nm is available for CALIPSO (Cattrall et al., 2005). The link between the two databases will be addressed at a later stage. A 'Scene Classification Algorithm' (SCA) at 50-km scale will provide with a classification of the atmospheric components detected in each range bin (see the list in Fig. 3). Currently under development, it combines Lidar and meteorological information. Notice that ADM-Aeolus will provide with limited information as presented on Table 2, so the SCA does not rely on synergism with other on-board measurements. The SCA is based on the backscatter-to-extinction ratio $k_{p,i}$, for the values are quite different for aerosols and clouds (Carier et al., 1967; Evans, 1988; Ackerman, 1997; Noel et al., 2001). In addition, temperature is an efficient criterion to discriminate between liquid water and ice crystal clouds. Above 0 °C marks the occurrence of liquid water clouds only and below –40°C only ice clouds (Bailey and Hallet, 2004). Further discrimination may be provided by the 3.8-km scale signal variability and the $\mathrm{LOD}_{p,i}$. The SCA will be upgraded using contemporary observations by other satellites.

Table 2 is a comparison of performances for ADM-Aeolus and CALIPSO according to the measurements performed by the two missions. The CALIPSO payload combines three instruments: CALIOP a SEBL, an Infrared Imager (IIR) and a Wide-Angle Camera (WAC).

4. Bin-accumulated signals

The ALADIN profiles will be built-up by analogue on-board accumulation over 25 vertical range bins of 500–2000 m of depth. Changing from Lidar range R to altitude z, the bin-accumulated Rayleigh $S_{m,i}$ and Mie $S_{p,i}$ signals for the range bin i are

$$S_{m,i} = \int_{z_{i-1}}^{z_i} s_m(y)\,\mathrm{d}y \tag{4a}$$

$$S_{p,i} = \int_{z_{i-1}}^{z_i} s_p(y)\,\mathrm{d}y. \tag{4b}$$

The altitudes z_i and z_{i-1} are the upper and lower boundaries of range bin i. The relationship between z and R is $z = (R_0 - R)\cos\theta$, R_0 is the range to the surface. In principle, the range bins of the Rayleigh (m) and Mie (p) channels could be different, as shown on Fig. 1, but it still needs to be defined according to current studies under progress at ESA. Here, they are set equal

for the sake of simplicity and for synergism between the two channels in order to derive $k_{p,i}$ (see Section 7). Now, starting from eqs (3a), (3b), (4a) and (4b) can be written for the range bin i as follows

$$S_{m,i} = K_m(\nu)\, T_{p,[\mathrm{sat},i]} T_{m,[\mathrm{sat},i]} \int_{z_{i-1}}^{z_i} \mathrm{d}y\, \frac{\beta_m(y)}{\left(R_0 - \frac{y}{\cos\theta}\right)^2} \times \exp\left[-\int_{z_{i-1}}^{y} \frac{2}{\cos\theta} [\alpha_m(x) + \alpha_p(x)]\, \mathrm{d}x \right] \quad (5a)$$

$$S_{p,i} = K_p(\nu)\, T_{p,[\mathrm{sat},i]} T_{m,[\mathrm{sat},i]} \int_{z_{i-1}}^{z_i} \mathrm{d}y\, \frac{\beta_p(y)}{\left(R_0 - \frac{y}{\cos\theta}\right)^2} \times \exp\left[-\int_{z_{i-1}}^{y} \frac{2}{\cos\theta} \left[\alpha_m(x) + \alpha_p(x)\right]\, \mathrm{d}x \right]. \quad (5b)$$

The instrumental factors $K_m(\nu)$ and $K_p(\nu)$depend slightly on the Doppler frequency shift ν, that is, radial velocity (Flamant et al., 2005). This effect will be taken into consideration by a proper calibration on the ground before launch (work under progress at ESA). The factors $T_{m,[\mathrm{sat},i]}$ and $T_{p,[\mathrm{sat},i]}$ are the two-way transmissions from the satellite (at height $h_0 = 400$ km) to z_i, the upper boundary of the ith range bin of interest, as follows

$$T_{m,[\mathrm{sat},i]} = \exp\left[-\int_{z_i}^{h_0} \frac{2}{\cos\theta} \alpha_m(y)\, \mathrm{d}y \right] \quad (6a)$$

$$T_{p,[\mathrm{sat},i]} = \exp\left[-\int_{z_i}^{h_0} \frac{2}{\cos\theta} \alpha_p(y)\, \mathrm{d}y \right]. \quad (6b)$$

In the upper atmosphere, θ may be considered as constant. In the lower atmosphere, the local elevation angleθ_i will be provided by range bin as L1B data. It is assumed that range bin #1, the closest to the surface, does not contain a surface echo. The additional complexity will be taken into account at a later stage of the L2A processor.

The inherent cross-talk between the Rayleigh and Mie channels, mentioned in Section 2, introduces four new instrumental factors in eqs (5a) and (5b), instead of two, and both Rayleigh ($S_{m,i}$) and Mie ($S_{p,i}$) signals account for scattered light by molecules (β_m) and particles (β_p). However, for the new set of two equations linking the bin-accumulated signals to the two variables of interest (i.e. light scattered by molecules and particles) is linear, it can be solved analytically. In practice, the unwanted contribution is subtracted (Mie from Rayleigh, Rayleigh from Mie). From on, provided the additional instrumental complexity is properly calibrated, the mathematical problem goes back to initial eqs (5a) and (5b). The new processing algorithm is presented in Section 5. An example of retrievals accounting for cross-talk is presented in Section 6.

In order to illustrate that the significant attenuation within a range bin changes the nature of the problem and calls for a new processing algorithm, we present numerical simulations of ADM-Aeolus signals in Fig. 4. It considers a cirrus layer between 10 and 12 km and aerosols in the atmospheric boundary layer between 0 and 2 km (see panel a). Bin-accumulated signals result in step like profiles, as displayed on panel (3b) for the Rayleigh channel and on panel (3c) for Mie channel. The range bins for each channel are distributed as shown in Fig. 1. We notice that changes in the range bin depth ($z_i - z_{i-1}$) result in discontinuities in the profiles (see Rayleigh and Mie profiles at 16 km and at 2.5 and 9 km, respectively).

Figure 5 presents in more details the bin-accumulated signal in the Rayleigh channel with only a cirrus cloud (10–12 km). The bin-accumulated signals without and with the cirrus cloud are displayed as black and grey dashed lines, respectively. For comparison, the corresponding range resolved molecular signal without and with the cirrus cloud are shown as solid black and grey lines, respectively. The dashed grey line shows a significant attenuation in the two successive range bins.

Using a normalized integrated two-way transmission (NITWT_i), a simple solution can be derived between an observation $S_{m,i}|_{\mathrm{obs}}$ and a calculated bin-accumulated signal for molecules only $S_{m,i}|_{\mathrm{cal}}$. From the range bin i, it expresses

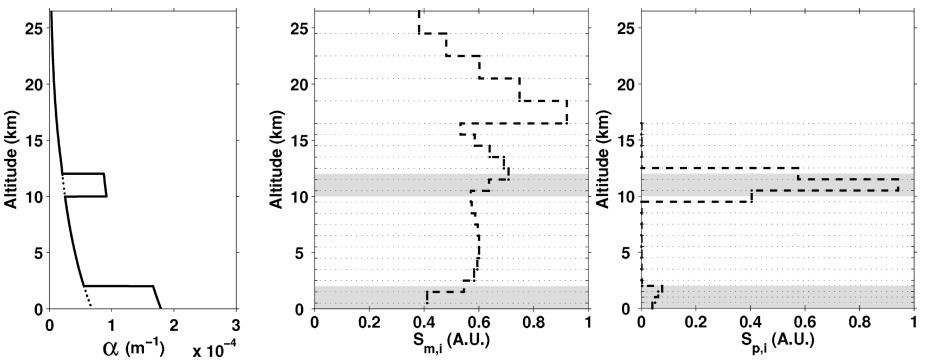

Fig. 4. Simulated bin-accumulated HSRL signals in arbitrary units (AU) as a function of altitude. Panel (a) atmospheric condition: a cirrus cloud is present between 10 and 12 km whereas the atmospheric boundary layer height is 2 km. The total extinction coefficient ($\alpha_p + \alpha_m$) is displayed as a solid line and α_m as a dotted line. Shaded grey areas outline the location of the two particle layers. Panel (b) bin-accumulated signal in Rayleigh channel $S_{m,i}$ and panel (c) range-accumulated signal in Mie channel $S_{p,i}$.

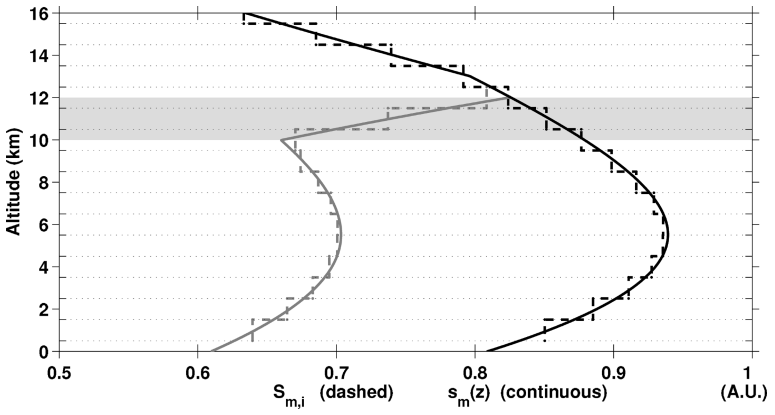

Fig. 5. Comparison of bin-accumulated and range resolved Rayleigh channel signals without (black) and with (grey) a cirrus cloud between 10 and 12 km. Dashed lines are the accumulated molecular signal $S_{m,i}$ in vertical range bins and continuous lines are the range resolved molecular signals $s_m(z)$. Simulations consider signals at 355 nm. Shaded grey area outlines the location of the cirrus layer. Despite $S_{m,i}$ and $s_m(z)$ are different (different units), they are plotted with the same scale for convenience. A normalizing factor of $(z_i - z_{i-1})$ was applied to $S_{m,i}$.

as

$$\mathrm{NITWT}_i = \frac{S_{m,i}|_{\mathrm{obs}}}{S_{m,i}|_{\mathrm{cal}}}. \tag{7}$$

At any time, using the L1B like-data and the auxiliary meteorological information (i.e. pressure and temperature profiles), the quantity NITWT_i may be calculated. Furthermore, we may explicit the numerator and the denominator of eq. (7) using the so-called 'mean value equation', as follows

$$S_{m,i}|_{\mathrm{obs}} = \int_{z_{i-1}}^{z_i} s_m(y)|_{\mathrm{obs}}\,\mathrm{d}y = s_m(z_k)\,|_{\mathrm{obs}} \times \int_{z_{i-1}}^{z_i} \mathrm{d}y = s_m(z_k)|_{\mathrm{obs}}\,(z_i - z_{i-1}) \tag{8a}$$

$$S_{m,i}|_{\mathrm{cal}} = \int_{z_{i-1}}^{z_i} s_m(y)|_{\mathrm{cal}}\,\mathrm{d}y = s_m(z_l)|_{\mathrm{cal}} \times \int_{z_{i-1}}^{z_i} \mathrm{d}y = s_m(z_l)|_{\mathrm{cal}}(z_i - z_{i-1}). \tag{8b}$$

The altitudes z_k and z_l are unknown and they verify $z_{i-1} \le z_l \le z_i$ and $z_{i-1} \le z_k \le z_i$. In the example of Fig. 5, these conditions are clearly observed. In the step-like profiles, the mean values in each range bin match the continuous profiles at a certain unknown altitude. For the range bins without particles, it results that $z_k = z_l$. However, when particles affect the atmospheric transmission, then $z_k \neq z_l$. Using eqs (8a) and (8b) in eq. (7), it comes

$$\mathrm{NITWT}_i = \frac{S_{m,i}|_{\mathrm{obs}}}{S_{m,i}|_{\mathrm{cal}}} = \frac{s_m(z_k)|_{\mathrm{obs}}}{s_m(z_l)|_{\mathrm{cal}}}. \tag{9a}$$

Note $s_m(z_k)|_{\mathrm{obs}}$ is not accessible to the measurement for ADM-Aeolus. Now, using eq. (3a) with altitude z instead of range R and $\theta_i \cong \theta$, eq. (9a) becomes

$$\mathrm{NITWT}_i = \frac{\beta_m(z_k)}{\beta_m(z_l)} \left(\frac{R_0 - \frac{z_l}{\cos\theta_i}}{R_0 - \frac{z_k}{\cos\theta_i}} \right)^2 T_{p,[\mathrm{sat},i]} \times \exp\left\{ -\frac{2}{\cos\theta_i} \left[\int_{z_{i-1}}^{z_k} \alpha_p(y)\,\mathrm{d}y + \int_{z_l}^{z_k} \alpha_m(y)\,\mathrm{d}y \right] \right\}. \tag{9b}$$

The difference between z_k and z_l is small for low $\mathrm{LOD}_{p,i} = \int_{z_{i-1}}^{z_i} \alpha_p(x)\,\mathrm{d}x$ (see Fig. 5). Neglecting the residual molecular attenuation and approximating $z_k \cong z_l$, eq. (9b) writes

$$\mathrm{NITWT}_i \cong T_{p,[\mathrm{sat},i]} \exp\left\{ -\frac{2}{\cos\theta_i} \left[\int_{z_{i-1}}^{z_k} \alpha_p(y)\,\mathrm{d}y \right] \right\}. \tag{9c}$$

This equation does not involve the local optical depth $\mathrm{LOD}_{p,i}$ nor a mean extinction coefficient $\alpha_{p,i}$ and z_k is unknown. A solution requires an additional assumption on the range bin filling. For a homogeneous particle layer filling entirely a given range bin [i.e. $\alpha_p(z_{i-1} \le z \le z_i) \cong \alpha_{p,i}$, using Taylor expansion for small $\mathrm{LOD}_{p,i}$, one can show that $z_k \cong (z_i + z_{i-1})/2$. Accordingly, eq. (9c) becomes

$$\mathrm{NITWT}_i \cong T_{p,[\mathrm{sat},i]} \exp\left[-\frac{2}{\cos\theta_i} \frac{(z_i - z_{i-1})}{2} \alpha_{p,i} \right]. \tag{9d}$$

And the mean extinction coefficient is

$$\alpha_{p,i} \cong \frac{\cos\theta_i}{(z_i - z_{i-1})} Ln \left[\frac{T_{p,[\mathrm{sat},i]}}{\mathrm{NITWT}_i} \right]. \tag{9e}$$

A simple solution (eqs 9d and 9e) has been derived according to the three assumptions: (i) low $\mathrm{LOD}_{p,i}$, (ii) homogeneous particle layers and (iii) total filling of the range bins. In that case, the particle transmission (see eq. 9c) looks like a standard transmission, but for half the range bin only (i.e. between $(z_i + z_{i-1})/2$ and z_{i-1}). The quantity $T_{p,[\mathrm{sat},i]}$ may be computed in successive steps from the useful top range bin #23 using eq. (6b). In the next section, a new processing algorithm is proposed that does not require assumptions on attenuation nor complete filling of the range bins.

5. Processing algorithm for Rayleigh channel

In this section, a new solution for the Rayleigh channel is proposed. It considers (i) any value of local optical depth $\mathrm{LOD}_{p,i}$, (ii) partial filling and (iii) homogeneous particles layers. It will be shown later that partial filling considerations could improve the effective vertical resolution by a factor two to four.

We derive the new solution starting from eq. (7), written as

$$\mathrm{NITWT}_i = \frac{K_m(\nu)}{K_m(\nu)} T_{p,[\mathrm{sat},i]} \frac{\int_{z_{i-1}}^{z_i} \mathrm{d}y \, \frac{\beta_m(y)}{\left(R_0 - \frac{y}{\cos\theta_i}\right)^2} \, \exp\left\{-\frac{2}{\cos\theta_i} \int_{z_{i-1}}^{y} \left[\alpha_m(x) + \alpha_p(x)\right] \mathrm{d}x\right\}}{\int_{z_{i-1}}^{z_i} \mathrm{d}y \, \frac{\beta_m(y)}{\left(R_0 - \frac{y}{\cos\theta_i}\right)^2} \, \exp\left[-\frac{2}{\cos\theta_i} \int_{z_{i-1}}^{y} \alpha_m(x) \, \mathrm{d}x\right]}. \tag{10}$$

Limited variations over a range bin of the molecular and range squared terms enable to take them out of the integrals at the numerator and denominator. It results

$$\frac{1}{T_{p,[\mathrm{sat},i]}} \mathrm{NITWT}_i = \frac{1}{(z_i - z_{i-1})} \int_{z_{i-1}}^{z_i} \mathrm{d}y \;\; \exp\left[-\frac{2}{\cos\theta_i} \int_{z_{i-1}}^{y} \alpha_p(x) \, \mathrm{d}x\right]. \tag{11}$$

For the particular case of total filling of a range bin by a particle layer of constant extinction coefficient $\alpha_{p,i}$, eq. (11) may be solved analytically to give

$$\frac{1}{T_{p,[\mathrm{sat},i]}} \mathrm{NITWT}_i = \frac{1}{2\ \mathrm{SLOD}_{p,i}} \left[1 - \exp\left(-2\ \mathrm{SLOD}_{p,i}\right)\right], \tag{12a}$$

where $\mathrm{SLOD}_{p,i}$ is the particle slant local optical depth as $\mathrm{SLOD}_{p,i} = (z_i - z_{i-1})\, \alpha_{p,i}/\cos\theta_i$.

For partial filling by one single homogeneous layer between altitudes z_a and z_b such that $z_{i-1} \le z_a \le z_b \le z_i$, eq. (11) writes

$$\frac{1}{T_{p,[\mathrm{sat},i]}} \mathrm{NITWT}_i = \frac{(z_i - z_b)}{(z_i - z_{i-1})} + \frac{(z_b - z_a)}{(z_i - z_{i-1})} \frac{1}{2\mathrm{SLOD}_{p,[a,b]}} \times \left[1 - \exp\left(-2\mathrm{SLOD}_{p,[a,b]}\right)\right] + \frac{(z_a - z_{i-1})}{(z_i - z_{i-1})} \exp\left[-2\mathrm{SLOD}_{p,[a,b]}\right]. \tag{12b}$$

If $z_a = z_{i-1}$ and $z_b = z_i$, eq. (12b) is identical to (12a). Implicit eqs (12a) and (12b) may be solved by successive iterations in order to minimize the difference between the right- and left-hand terms. Using the left hand term as reference, the difference can be positive or negative, corresponding to a small underestimation or overestimation of the local optical depth, respectively. For a single homogeneous particle layer, between any z_a and z_b within the boundaries of range bin i, the Rayleigh channel retrieval of the local optical depth $\mathrm{LOD}^R_{p,i}$ is finally,

$$\mathrm{LOD}^R_{p,i} = \mathrm{SLOD}_{p,[a,b]} \cos\theta_i. \tag{12c}$$

The $\mathrm{LOD}^R_{p,i}$ retrieved from eqs (12b) and (12c) depends not only on the slant optical depth $\mathrm{SLOD}_{p,[a,b]}$ but also on the location of the particle layer in the range bin. Considering two extreme cases, a very thin layer located either at the top: $z_b = z_i$ and $z_a \cong z_i$ (see eq. 13a) or bottom: $z_b \cong z_{i-1}$ and $z_a = z_{i-1}$ (see eq. 13b) of a range bin, one can write

$$\frac{1}{T_{p,[\mathrm{sat},i]}} \mathrm{NITWT}_i \cong \exp\left[-2\ \mathrm{SLOD}_{p,\mathrm{top}}\right] \tag{13a}$$

$$\frac{1}{T_{p,[\mathrm{sat},i]}} \mathrm{NITWT}_i \cong 1. \tag{13b}$$

Despite the local optical depth are equal, the two eqs (13a) and (13b) are quite different. An incorrect assumption on the filling of the range bins (e.g. total filling when particle layers are thinner than the range bins) may then result in significant bias. Moreover, the right-hand term of eq. (13b) is nearly equal to unity, for only a very small fraction of the signal is attenuated. It results in an apparent contradiction between the Feature Finder Algorithm that indicates the presence of a significant particle layer in the range bin while the Rayleigh Processing algorithm could indicate a negligible particle local optical depth. The combination of the two pieces of information tells us that it is a thin layer at the bottom of the range bin. In future works, cross-information algorithms will be implemented in the L2A processor.

In order to limit the number of solutions to be tested, we divide the range bins into four subbins and we consider only one layer by range bin. The various filling cases (FC) to be used in this study are displayed on Fig. 6. They correspond to seven cases: an entire range bin or total filling (#1), top and bottom halves (#2 and #3), upper top, mid-top, mid-bottom and lower bottom quarters (#4, #5, #6 and #7).

Once the Feature Finder algorithm has identified the range bins containing particles, the best approximation among the possible FC is to be determined. In order to make a decision, a so-called CC is used. From eq. (12b), we define it as,

$$CC_i = \frac{1}{T_{p,[\mathrm{sat},i]}} \mathrm{NITWT}_i, \tag{14a}$$

where $T_{p,[\mathrm{sat},i]}$ and NITWT_i are calculated using eqs (6b) and (7), respectively. The CC_i computed in range bin i is intended to certify all FC_{i+1} and $\mathrm{LOD}_{p,i+1}$ retrieved in the above range bins (from the upper most bin #24 down to $i + 1$). The NITWT_i may be computed directly from L1B observed and simulated signals. On the contrary, the estimation of $T_{p,[\mathrm{sat},i]}$ relies on the previously retrieved particle optical depth in the range bin i+1 and above. From eq. (6b), the two-way particular transmission

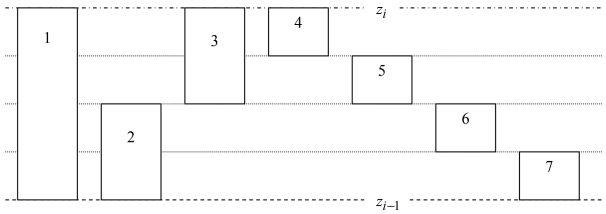

Fig. 6. Filling cases (FC) considered for numerical simulations: total filling and various partial fillings of a range bin by one homogeneous particle layer (seven cases).

from the satellite to z_i equals

$$T_{p,[\mathrm{sat},i]} = \exp\left[-\sum_{k=i+1}^{23} \frac{2}{\cos\theta_k} \mathrm{LOD}_{p,k} \right] + T_{p,[\mathrm{sat},24]}. \qquad (14b)$$

For the range bins $i+1$ to #23, the local optical depths $\mathrm{LOD}_{p,k}$ were obtained by iteratively solving eq. (12b) for the chosen FC_k. We may then only calculate CC_i for the range bin i, once we had calculated $\mathrm{LOD}_{p,\geq i+1}$ for the chosen $\mathrm{FC}_{\geq i+1}$ in the range bin i+1 and above. $\mathrm{LOD}_{p,24}$ and $\mathrm{LOD}_{p,25}$ are assumed to be equal to zero. Then, $T_{p,[\mathrm{sat},24]}$ is obtained by using range bin #24 for calibration of $S_{m,i}|_{\mathrm{calc}}$, that is, the ratio between $S_{m,24}|_{\mathrm{obs}}$ and $S_{m,24}|_{\mathrm{cal}}$ is the normalizing factor $T_{p,[\mathrm{sat},24]}$ (see eq. 5a). Range bin #25 was previously used for instrumental purpose during L1B processing.

Retrievals will provide with the filling case FC_i and the local optical depth $\mathrm{LOD}_{p,i}$ for each range bin i. For a given profile $S_{m,i}|_{\mathrm{obs}}$, each one of the filling cases are tested following a tree-like structure. The procedure starts at the upper most range bin i where particles where detected by the Feature Finder algorithm, where it calculates $\mathrm{LOD}_{p,i}$ for all possible FC_i and verifies CC_{i-1} in the range bin below. Depending on CC_{i-1} and for an uncertainty ε, three possible decisions may be taken:

(i) *On-going condition*: If $\mathrm{CC}_{i-1} < 1-\varepsilon$, the so far retrieved $\mathrm{LOD}_{p,i}$ and chosen FC_p are considered as a possible solution. Processing *goes on* to the following range bin (i.e. it will calculate $\mathrm{LOD}_{p,i-1}$ for all possible FC_{i-1} and CC_{i-2} to make a new decision).

(ii) *Rejection condition*: If $\mathrm{CC}_{i-1} > 1+\varepsilon$, the assumed filling cases from the top range bin down to range bin i include at least one wrong FC and so wrong LOD_p. It underestimates the two-way transmission (eq. 6b). Then, the entire profile is *rejected*: all the chosen $\mathrm{FC}_{\geq i}$ above range bin i are discarded. Then the procedure starts again in the upper most range bin with a new FC.

(iii) *Acceptance condition*: If $CC_{i-1} = 1 \pm \varepsilon$, the optical depth is declared correct and the entire profile (down to $\mathrm{LOD}_{p,i}$) is *accepted* as a partial solution (i.e. between #23 and i).

Next, processing continues in the following range bins containing particles (i.e. $i-2$ or below), as identified by the Feature Finder algorithm. It provides with a solution down to the surface (i = #1). The error propagation due to numerical and physical approximations, as well as signal noise, is to be considered in the value of ε (a few percents).

Preliminary numerical tests using the procedure outlined above are presented in the next section. Furthermore, analytical and numerical tests concerning the impact of MSE on the new retrieval algorithms have been as well done. They showed that MSE in one range bin do not result in error propagation that may impact the retrieval into the next range bins and so on. In future works, the performance in case of MSE will be tested using Monte Carlo simulations for the Lidar signals.

6. Preliminary tests on Rayleigh Channel new processing algorithm

To test the performance of the new processing algorithm, numerical tests considering L1B like data simulated with low noise (high SNR) for 50-km bin-accumulated signals were used. Only digitalization and range bin position uncertainties were taken into account. Three examples will be presented. First, we simulated the Lidar signals considering two consecutive range bins #20 and #19 completely filled by particles (i.e. FC#1) and three optical depths (0.06, 0.30 and 1.00), equally split between the two range bins. As a sensitivity test, we processed the Lidar signals assuming various filling cases different from the input (see Table 3).

Table 4 compares the retrieved total optical depths ($\mathrm{OD} = \mathrm{LOD}_{p,20} + \mathrm{LOD}_{p,19}$) for each of the five test cases. The OD was only correct when the proper filling cases were used (see Table 3). In Test #4 (two thin particle layers at the bottom and at the top of each range bin), the biases were compensated and the OD approached the inputs.

In a second example, the L1B like data were simulated with a particle layer in range bin #20 with $\mathrm{LOD}_{p,20} = 0.30$ and FC_{20} = #7. Filling case #7 is the more difficult to address. In a blind test, the L1B like data were processed according to the seven filling cases of Fig. 6 and CC_i computed in range #19 and #18. First, the processing algorithm started in bin #20 with FC_{20} = #1 (complete filling) and then tried the seven filling cases in bin #19. Second, it tried FC_{20} = #2 and then the seven filling factors in #19, and so on until filling case #7 was tried in bin #20 and the seven filling cases in #19 as before. Table 5 presents the results. Only the best results for range bin #19 are displayed.

Table 3. Filling cases (see Fig. 6) in range bins #20 and #19 used to test the sensitivity of the Rayleigh channel processing algorithms. Test case #1 corresponds to the filling cases considered for simulation of the bin-accumulated signals and the other four columns to incorrect filling assumptions

Range bin	Test #1	Test #2	Test #3	Test #4	Test #5
#20	FC #1	FC #2	FC #3	FC #4	FC #5
#19	FC #1	FC #3	FC #2	FC #7	FC #6

Table 4. Total optical depth (OD) retrieved when the processing algorithm assumed the five different test cases presented in Table 3. Signals were simulated considering the filling cases of Test #1

Input	Output				
	Test #1	Test#2	Test #3	Test #4	Test #5
OD = 0.06	0.060	0.091	0.046	0.054	0.107
OD = 0.30	0.30	0.48	0.23	0.28	0.59
OD = 1.00	0.99	2.12	0.82	1.04	3.12

Table 5. Example of 'Processing Algorithms' results applied to L1B like data simulated with a particle layer in the range bin #20, with $\mathrm{LOD}_{p,20} = 0.30$ and filling case #7 (input case). Processing considered the seven filling cases presented on Fig. 6. Only the best results for range bin #19 are displayed. The on-going, rejection and acceptance conditions are indicated by '⇒Go', '⇒Stop' and '⇒OK', respectively.

Range bin		Input	Outputs							
			Processing Algorithms (Rayleigh channel)							Feature Finder
#20	FC_{20}	#7	#1	#2	#3	#4	#5	#6	#7	Particles
	$\mathrm{LOD}_{p,20}$	0.30	0.07	0.14	0.04	0.04	0.05	0.09	0.32	
#19	FC_{19}	–	#4	#4	#4	#4	#4	#4	–	Empty
	$\mathrm{LOD}_{p,19}$	0	0.28	0.19	0.30	0.31	0.29	0.25	–	
	CC_{19}	1	0.527 ⇒Go	0.673 ⇒Go	0.527 ⇒Go	0.525 ⇒Go	0.546 ⇒Go	0.599 ⇒Go	1.039 ⇒OK	
#18	CC_{18}	1	1.11 ⇒Stop	1.07 ⇒Stop	1.12 ⇒Stop	1.13 ⇒Stop	1.12 ⇒Stop	1.09 ⇒Stop	–	Empty
OD		0.30	0.35	0.33	0.34	0.35	0.34	0.34	0.32	

The CC_i in range bin #19 (#18) was the NITWT_{19} (NITWT_{18}) corrected for attenuation by particles in range bin #20 (#19). The NITWT_i equalled 1 in the absence of particle layers. The acceptance condition was only met for FC_{20}#7 column, used to simulate the Lidar signal. Filling case 7 was the most difficult to handle as said before and at best $\mathrm{CC}_{19} = 1.036$. The new processing algorithm for the Rayleigh channel performed well and it enabled to retrieve (i) the optical depth (+6%), (ii) the right range bin filled with particles and (iii) the filling case.

As said before, the apparent contradiction between information provided by the Feature Finder and processing algorithms can be used to improve the overall processing and Scene Classification (to be conducted as a future work). Table 5 shows that the Feature Finder would have indicated a particle layer in range bin #20 and no particles in #19 and #18, whereas the processing algorithm based on wrong FC_{20} assumption retrieved most of the optical depth in range bin #19.

The third test is presented in Fig. 7. It is a comparison between L1B like data with and without cross-talk in panels (a) and (c), respectively, for a cloud layer (in grey) between 5.35 and 6.85 km and OD = 0.30. As shown, the particle layer was sampled in three range bins with filling cases #4, #1 and #7, respectively. The retrievals are, respectively, displayed in panels (b) and (d). The input is the shaded grey area. Before processing, the Rayleigh channel signal in panel (c) was corrected from cross-talk by the procedure mentioned in Section 4, including noise in calibrations. The retrievals using the 'simple solution' which only considers total filling (eq. 9d) is displayed as solid thin line. The wrong filling assumption in the upper range bin propagated a bias that could reach more than 40% for the following range bins. Retrievals using the new processing algorithms (eq. 12b) are displayed as dashed line. They both matched the input extinction coefficient profile used as input.

7. Processing algorithm for Mie channel and synergism between the two channels

The Mie channel is used for the Feature Finder and the signal Processing Algorithms (Fig. 3). In this section, we present the processing algorithm for the Mie channel in the absence of information from the Rayleigh channel (Section 7.1) and then the synergism between the two channels when the setting of the range bins are identical (Section 7.2).

7.1. Mie channel standing alone

One starts from eq. (5b). Using $\beta_{p,i} = k_{p,i}\alpha_{p,i}$, where $k_{p,i}$ is a mean value over range bin i, it comes

$$S_{p,i} = T_{p,[\mathrm{sat},i]}\, T_{m,[\mathrm{sat},i]}\, K_p(\nu) k_{p,i} \int_{z_{i-1}}^{z_i} \mathrm{d}y\, \frac{\alpha_p(y)}{\left(R_0 - \frac{y}{\cos\theta}\right)^2} \times \exp\left\{-\frac{2}{\cos\theta}\int_{z_{i-1}}^{y}\left[\alpha_m(x) + \alpha_p(x)\right]\mathrm{d}x\right\}. \quad (15a)$$

Taking out the molecular and range squared terms as before, a standard solution (Platt, 1973) is derived with new variable $U = \int_{z_{i-1}}^{y} \alpha_p(x)\,\mathrm{d}x$ and $\mathrm{d}U = \alpha_p(y)\,\mathrm{d}y$. The analytic solution is

$$S_{p,i} = T_{p,[\mathrm{sat},i]}\, T_{m,[\mathrm{sat},i]}\, \frac{\exp(-\mathrm{SLOD}_{m,i})}{\left[R_0 - \frac{(z_i + z_{i-1})}{2\cos\theta_i}\right]^2} K_p(\nu) \times \cos\theta_i\, \frac{k_{p,i}}{2}\, [1 - \exp(-2\mathrm{SLOD}_{p,i})], \quad (15b)$$

where $\mathrm{SLOD}_{m,i}$ and $\mathrm{SLOD}_{p,i}$ are the local optical depth, respectively, for molecules and particles and θ_i is provided as L1B data. Following the same reasoning of eq. (9d) for molecules, the factor $\exp(-\mathrm{SLOD}_{m,i})$ considers only half the two-way transmission. As the Mie channel stands alone, $k_{p,i}$ needs to be known a priori. In case of MSE, a correcting factor (η) occurs in eq. (15a) in front of α_p as discussed

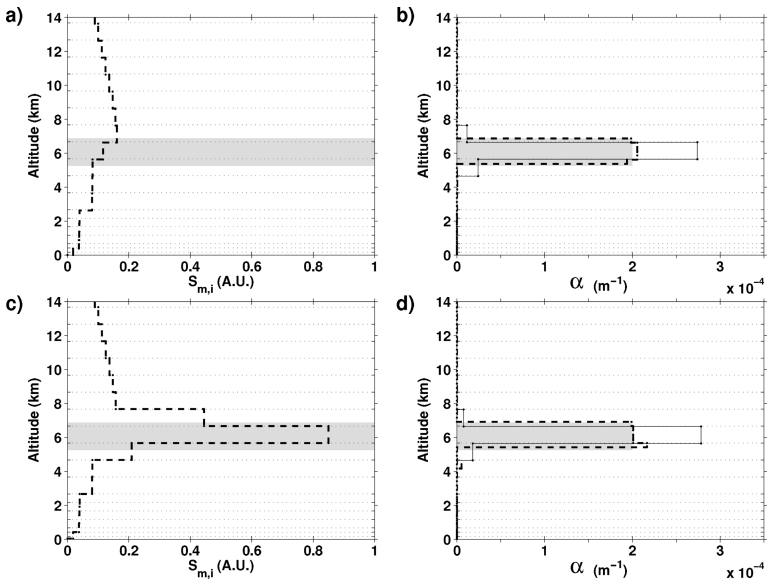

Fig. 7. Comparison between L1B like data with and without cross-talk in panels (a) and (c) for a cloud layer (in grey) between 5.35 and 6.85 km and OD = 0.30. The retrievals are displayed in panels (b) and (d). The input for simulation is the shaded grey area. The retrievals using the new processing algorithm (eq. 12b) are displayed as dashed lines. The retrievals using a simple solution (eq. 9d) are shown as solid thin lines.

in Section 1. It applies twice in eq. (15b):$(k_{p,i}/2\eta)$ instead of $(k_{p,i}/2)$ and $[1-\exp(-2\eta\ \mathrm{SLOD}_{p,i})]$ instead of $[1-\exp(-2\mathrm{SLOD}_{p,i})]$. However, for small SLOD, a first-order Taylor expansion shows that the two MSE correction factors η cancel and have no impact on the $\mathrm{SLOD}_{i,p}$ retrieval. Equation (15b) can then be written as

$$S_{p,i} \cong T_{p,[\mathrm{sat},i]}\ T_{m,[\mathrm{sat},i]}\ \frac{\exp(-\mathrm{SLOD}_{m,i})}{\left[R_0-\frac{(z_i+z_{i-1})}{2\cos\theta_i}\right]^2}\ K_p(\nu)\ \ k_{p,i}\ \mathrm{LOD}_{p,i} \tag{15c}$$

and the Mie Channel local optical depth retrieval $\mathrm{LOD}^M_{p,i}$ is

$$\mathrm{LOD}^M_{p,i} \cong \frac{S_{p,i}}{K_p(\nu)\ \ k_{p,i}}\ \frac{\left[R_0-\frac{(z_i+z_{i-1})}{2\ \cos\theta_i}\right]^2}{T_{p,[\mathrm{sat},i]}\ T_{m,[\mathrm{sat},i]}}\ \exp\big(\mathrm{SLOD}_{m,i}\big)\,. \tag{16a}$$

In the general case, we may solve eq. (15b) to obtain

$$\mathrm{LOD}^M_{p,i} = \left(-\frac{\cos\theta_i}{2}\right)\ln\left\{1-\frac{2}{\cos\theta_i}\,\frac{S_{p,i}}{K_p(\nu)\ k^{\mathrm{aux}}_{p,i}} \times\frac{\left[R_0-\frac{(z_i+z_{i-1})}{2\cos\theta_i}\right]^2}{T_{p,[\mathrm{sat},i]}\ T_{m,[\mathrm{sat},i]}}\exp\big(\mathrm{SLOD}_{m,i}\big)\right\}. \tag{16b}$$

As before, the molecular transmission $T_{m,[\mathrm{sat},i]}$ is calculated using auxiliary meteorological data, that is, pressure and temperature profiles. The transmission for particles is computed from previous range bins (from #23 to $i+1$).

The retrieval of $\mathrm{LOD}^M_{p,i}$ depends on the choice of $k^{\mathrm{aux}}_{p,i}$ from an auxiliary data set (see Fig. 3). Also, for the transmission for particles $T_{p,[\mathrm{sat},i]}$ is computed using LOD in previous bins, then the errors in the choice of $k^{\mathrm{aux}}_{p,i}$ and the inherent MSE (i.e. in case of large particles and high OD) may result in bias propagation through the retrieved profiles (this point will be further addressed in a future study). As mention in Table 2, it is a source of ambiguity for CALIPSO or any SEBL retrievals, operating from the ground or in the air. Moreover, a determination of $K_p(\nu)$ in absolute value is needed. Notice that $K_p(\nu)$ and $k_{p,i}$ are inextricably connected in eqs (15) and (16). $K_p(\nu)$ needs a careful calibration on ground before launch (work in progress at ESA). In space, it could be done using calibrated surface returns (but reflectance needs to be known) and strong cloud returns (k_p is rather stable and well known for dense water clouds).

7.2. Synergism between Rayleigh and Mie channels

In order to derive a mean $k_{p,i}$ for each range bin i, we may combine the two independent $\mathrm{LOD}_{p,i}$ retrieved from Rayleigh and Mie channels. Using the Rayleigh retrieval $LOD^R_{p,i}$ in eq. (15b) enables to calculate the 'Rayleigh + Mie' mean $k^{R+M}_{p,i}$ over range bin i as follows

$$k^{R+M}_{p,i} = \frac{2}{\cos\theta_i}\,\frac{S_{p,i}}{K_p(\nu)}\,\frac{\left[R_0-\frac{(z_i+z_{i-1})}{2\cos\theta}\right]^2}{T_{p,[\mathrm{sat},i]}T_{m,[\mathrm{sat},i]}} \times\frac{\exp\big(\mathrm{SLOD}_{m,i}\big)}{1-\exp\big(-2\ \mathrm{SLOD}^R_{p,i}\big)}. \tag{17a}$$

In case of MSE in bin i, the retrieval of $k^{R+M}_{p,i}$ should not be biased for small LOD because the two channels share the same FOV. Considerations for larger LOD and occurrence of significant MSE will be addressed in a future study.

When $k_{p,i}^{R+M}$ is known, the mean scattering ratio for the range bin i may be derived by

$$R_{\mathrm{sca},i}^{R+M} = 1 + k_{p,i}^{R+M} \frac{\mathrm{LOD}_{p,i}^{R}}{\mathrm{LOD}_{m,i}} \tag{17b}$$

Equation (17b) can be written in LOD or SLOD as well. The scattering ratio derived using (17b) will be compared to the value derived using the Feature finder algorithm (see Section 3). In presence of MSE the scattering ratio (see eq. 17b) should not be biased. In principle, the MSE correcting factors for backscatter-to-extinction ratio and particle local optical depth cancel.

8. Summary and conclusion

This paper is intended to demonstrate the potential of ADM-Aeolus to derive spin-up products for clouds and aerosols using a high spectral resolution Lidar in the UV. We show that even if ADM-Aeolus is designed for wind application mainly, it can fulfil the objective satisfactorily. The proposed ADM-Aeolus L2A processor aims at retrieving the optical parameters of aerosol and cloud layers: (i) local optical depths or mean extinction coefficient by range bin, (ii) backscatter to extinction ratio and (iii) scattering ratio. The theoretical basis and first numerical tests were presented in the present paper. The algorithms usually used for range resolved signals are not applicable to ADM-Aeolus because of the coarse vertical resolution of the instrument. A new approach has been developed that does correctly account for the vertical bin accumulation and the possibility that a cloud or aerosol layer may partially fill a range bin. The practical implementation of the processor requires precise calibration of ADM-Aeolus [characterization of instrumental parameters $k_m(\nu)$ and $k_p(\nu)$ and cross-talk partitioning]. These issues are under progress at ESA. The impact of the multiple scattering effects on the retrieval of local optical depth in a range bin has been discussed, but a more detailed analysis using Monte Carlo simulations of the Lidar signals is left to future works for completeness. Future upgrades the L2A processor will include an exhaustive set of partial filling cases. The apparent contradiction between the Feature Finder algorithm information and processing algorithms retrievals requires additional study. Cross-information processing will be addressed in future works. The optical products provided by ADM-Aeolus will extend the databases obtained by CALIPSO measurements and bridge the gap between CALIPSO and EARTH-CARE, the Lidar/Radar mission that ESA is preparing in the framework of Earth-Explorers program.

9. Acknowledgements

This work is supported by ESA under contract: Aeolus Level 1B/2A processor, 18366/04/NL/MM. The author would like to acknowledge the fruitful reviews and comments made by ESTEC/ESA personnel. The authors thank Sylvain Lassaut and Olivier Chomette for their support in the early phase of the study.

References

Ackerman, J. 1997. The extinction-to-backscatter ratio of tropospheric aerosol: a numerical study. *J. Atmos. Sci.* **15**, 1043–1050.

Bailey, M. and Hallett, J. 2004. Growth rates and habits of ice crystals between -20° and -70°C. *J. Atmos. Scie.*

Boley, C. D., Tenti, G. and Desai, R. C. 1972. Kinetic Models and Brillouin Scattering in a Molecular Gas. *Can. J. Phys.* **50**, 2158–2173.

Carier, L. W. G. A., Cato, K. J. and von, Essen 1967. The backscattering and extinction of visible and infrared radiation by selected major cloud models. *Appl. Opt.* **6**, 1209–1216.

Cattrall, C., Reagan, J., Thome, K. and Dubovik, O. 2005. Variability of aerosol and spectral lidar and backscatter and extinction ratios of key aerosol types derived from selected aerosol robotic network locations. *J. Geophys. Res.-Atmos.* **110**, D15, D15S11, Paper No. 10.1029/2004JD005124)

Chanin, M. L., Garnier, A., Hauchecorne, A. and Porteneuve, J. 1989. A Doppler lidar for measuring winds in the middle atmosphere. *Geophys. Res. Lett.* **16**, 1273–1276.

ESA 1999. The four candidate Earth Explorer core missions—Atmospheric Dynamics Mission. ESA report for mission selection. **ESA SP-1233**(4), 145 pp.

Evans, B. T. 1988. Sensitivity of the backscatter-to-extinction ratio to changes in optical properties: implications for lidar. *Appl. Opt.* **27**, 3299–3305.

Fernald, F. G., Herman, B. M. and Reagan, J. A. 1972. Determination of aerosol height distributions by lidar. *J. Appl. Meteorol.* **11**, 482–489.

Fernald, F. G. 1984. Analysis of atmospheric lidar observations – some comments. *Appl. Opt.* **23**, 652–653.

Flamant, P., Loth, C., Dabas, A., Denneulin, M.-L., Dolfi-Bouteyre, A. and co-authors. 2005. ILIAD: impact of line shape on wind measurements and correction methods. Final report ESTEC contract 1833404/NL/MM. 124 p.

Garnier, A. and Chanin, M. L. 1992. Description of a Doppler Rayleigh lidar for measuring winds in the middle atmosphere. *Appl. Phys.*, **B55**, 35–40.

Imaki, M., Takegoshi, Y. and Kobayashi, T. 2005. Ultraviolet High-spectral-resolution Lidar with Fabry-Perot filter for accurate measurement of extinction and lidar ratio. *Jpn. J. Appl. Phys.* **44**, 3063–3067.

Mitrescu, C. 2005. Lidar model with parameterized multiple scattering for retrieving cloud optical properties. *J. Quant. Spectrosc. Radiat. Trans.* **94**, 201–224.

Nicolas, F., Bissonnette, L. R. and Flamant, P. H. 1997. Lidar effective multiple-scattering coefficients in cirrus clouds. *Appl. Opt.* **36**, 3458–3468.

Noël, V., Ledanois, G., Chepfer, H. and Flamant, P. H. 2001 Computation of single-scattering matrix for non spherical particles randomly and horizontally oriented in space. *Appl. Opt.* **40**, 4365–4375.

Pan, X. G., Shneider, M. N. and Miles, R.B. 2004. Coherent Rayleigh-Brillouin scattering in molecular gases. *Phys. Rev. A* **69**, article #033814.

Platt, C.R.M. 1973. Lidar and radiometric observations of cirrus clouds, *J. Atmos. Sc.* **30**, 1191–1204.

Shipley, S. T., Tracy, D. H., Eloranta, E. W., Trauger, J. T., Sroga, J. T. and co-authors. 1983. High spectral resolution lidar to measure optical scattering properties of atmospheric aerosols. 1: theory and instrumentation. *Appl. Opt.* **22**, 3716–3724.

Stoffelen, A., Pailleux, J., Källén, E., Vaughan, J. M., Isaksen, L. and co-authors. 2005. The atmospheric dynamics mission for global wind measurement. Bull. *Amer. Meteorol. Soc.* **86**, 73–87.

Tenti, G., Boley, C. D. and Desai, R. C. 1974. On the kinetic model description of Rayleigh-Brillouin scattering from Molecular Gases. Canadian. *J. Phys.* **52**, 285–290.

Winker, D. M., Pelon, J. and McCormick,M. P. 2003. The CALIPSO mission: Spaceborne lidar for observation of aerosols and clouds. In *Lidar Remote Sensing for Industry and Environment Monitoring III*. Proc. SPIE **Volume 4893** (eds Singh, U. N., Itabe, T. and Lui, Z.), pp. 1–11. SPIE, Bellingham, WA.